atmosphere

MDPI

Article

Evapotranspiration Variations of the Minjiang River Basin in Southeastern China from 2000 to 2019

Yijin Lu [1], Yuanyuan Wang [1], Qun Liu [1,2,3,*], Xingwei Chen [1,2,3], Yuqing Zhang [4], Lu Gao [1,2,3], Ying Chen [1,2,3], Meibing Liu [1,2,3] and Haijun Deng [1,2,3,*]

1 National Demonstration Center for Experimental Geography Education, Fujian Normal University, Fuzhou 350007, China; luyijin2021@163.com (Y.L.); wyuanyuan2021@163.com (Y.W.); cxwchen215@fjnu.edu.cn (X.C.); gaolu@fjnu.edu.cn (L.G.); chenying@fjnu.edu.cn (Y.C.); lmb_18@163.com (M.L.)
2 Institute of Geography, Fujian Normal University, Fuzhou 350007, China
3 Fujian Provincial Engineering Research Center for Monitoring and Assessing Terrestrial Disasters, Fujian Normal University, Fuzhou 350007, China
4 School of Urban and Environmental Science, Huaiyin Normal University, Huai'an 223300, China; 8201711019@hytc.edu.cn
* Correspondence: liuqun@fjnu.edu.cn (Q.L.); denghj@fjnu.edu.cn (H.D.)

Abstract: Evapotranspiration is one of the critical processes in the terrestrial hydrological cycle, and the assessment of evapotranspiration is essential for understanding the regional hydrological cycle. In this study, the Minjiang River Basin, a typical watershed in the humid subtropical climate zone, is selected as the study region. The Penman-Monteith equation and the dual crop coefficient method are used to calculate the actual evapotranspiration (ET_a) at seven meteorological stations within the study basin. Meanwhile, the applicability of the Global Land Data Assimilation System-Noah (GLDAS-Noah) ET_a data in the Minjiang River Basin is evaluated based on stations P-M equation results, then to analyze the changes of the ET_a in the Minjiang River Basin from 2000 to 2019. The results show that the GLDAS-Noah ET_a data are well applicable in the Minjiang River Basin ($R^2 > 0.9$ and $NSE > 0.8$). The ET_a in the basin shows an increasing trend since 2000, and the increasing rate is 3.60 mm·yr^{-1} ($p < 0.01$). The seasonal variation results show that ET_a tends to increase in winter and spring, with increasing rates of 1.10 mm·yr^{-1} ($p < 0.01$) and 2.60 mm·yr^{-1} ($p < 0.01$), respectively, while the ET_a did not change significantly in summer and autumn. Annual air temperature has the largest effect on annual ET_a (59.6%), followed by precipitation at 33.9%. ET_a increased in spring was mainly influenced by increasing temperatures (89.4%) in the Minjiang River Basin from 2000 to 2019. The research results are of great benefit to further improve the understanding of ET_a variations in the basin under global warming.

Keywords: evapotranspiration; Penman-Monteith equation; GLDAS-Noah model; climate change; Minjiang river basin

check for updates

Citation: Lu, Y.; Wang, Y.; Liu, Q.; Chen, X.; Zhang, Y.; Gao, L.; Chen, Y.; Liu, M.; Deng, H. Evapotranspiration Variations of the Minjiang River Basin in Southeastern China from 2000 to 2019. *Atmosphere* **2022**, *13*, 562. https://doi.org/10.3390/atmos13040562

Academic Editor: Carlos E. Ramos Scharrón

Received: 30 December 2021
Accepted: 28 March 2022
Published: 30 March 2022

Publisher's Note: MDPI stays neutral with regard to jurisdictional claims in published maps and institutional affiliations.

Copyright: © 2022 by the authors. Licensee MDPI, Basel, Switzerland. This article is an open access article distributed under the terms and conditions of the Creative Commons Attribution (CC BY) license (https://creativecommons.org/licenses/by/4.0/).

1. Introduction

Evapotranspiration bridges land-atmosphere interactions and plays an essential role in regional hydrological cycle and water balance [1,2]. Changes in actual evapotranspiration (ET_a) are closely related to meteorological conditions (such as air temperature, precipitation, and wind speed) and surface characteristics (including soil moisture, crop type and growth status). These factors significantly change under climate change and human activities, thereby affecting ET_a [3,4]. ET_a is an essential factor affecting runoff, and its accurate estimation at the basin scale is crucial for further understanding hydrological cycle processes and water resource management, and even for promoting the sustainable development of water resources [5].

ET_a estimation methods mainly include traditional and remote sensing methods. Traditional methods for estimating ET_a include the water balance method [3], the Bowen

ratio-energy balance method [6], Penman-Monteith (P-M) equation [7], and the method proposed by Dalton (1802) reflecting the relationship between the surface evaporation rate and impact factors (atmospheric physical properties and physiological characteristics of vegetation) [8]. These methods have several advantages, i.e., simple structure, high accuracy, and relatively good applicability. However, they only perform well at the single-point and station scales [9], while the errors are relatively large at the regional scale. In the last 30 years, with the development of remote sensing technology with a high spatio-temporal resolution, it has been possible to quantitatively estimate the regional ET_a [10], with the advantages of all-weather, real-time and better accuracy. However, this technology is highly influenced by clouds, thus requiring validation by ground-based stations. In addition, land surface modeling and data assimilation, such as, the Global Land Data Assimilation System (GLDAS) model and reanalysis data (such as the ERA5 dataset), can also provide ET_a data. However, these estimates needs to be validated based on observations before application. Therefore, combining traditional methods with remote sensing methods, land surface process models and reanalysis data can improve the estimation accuracy of ET_a.

Under the background of global warming, ET_a changes show significant spatio-temporal differences in China [11]. ET_a in the northeastern part of the Songhua River Basin [12], the North China Plain [13] and the coastal region of southeastern China [14] have shown increasing trends. In the western, northern, and southeastern parts of the Loess Plateau, ET_a tended to decrease [15]. Tibetan Plateau averaged terrestrial ET_a increased significantly (1.87 mm yr^{-1}, $p < 0.001$) from 1982 to 2016 and is due primarily to precipitation increased [16]. The ET_a in Southwest China had tended to decrease from 1960 to 2013, mainly influenced by the shorter than solar radiation and lower wind speed [17]. The ET_a in arid Northwest China showed a decreasing trend from 1958 to 1993 and an increasing trend from 1994 to 2010, mainly closely related to the near-surface wind speed variation [18]. Liu et al. (2011) [19] revealed that the potential evapotranspiration (PET) in the basins of Southeast China showed a decreasing trend between 1960 and2007, which was most sensitive to changes in the maximum daily temperature. The regional differences in ET_a variability reflect regional hydrothermal conditions in the warming context and regional surface characteristics. Therefore, exploring ET_a variations can contribute to understanding the characteristics of regional hydrological changes in the warming context.

As the largest river of Fujian Province, the Minjiang River Basin (MRB) is of great importance to the economic, social, and ecological development of Fujian. In the past 20 years, notable warming in the MRB [20], and the frequency and intensity of successive autumn-winter-spring meteorological droughts in the basin have tended to increase [21]. The increase in the temperature and ET_a is likely one of the critical reasons for droughts in the MRB. However, current research results lack attention to ET_a variations in the MRB. There are only eight meteorological stations in the MRB, which makes it difficult to assess ET_a variations at the basin scale. Due to the complex and diverse topographic conditions in the basin, its middle and upper reaches usually experience cloudy and foggy weather, which seriously affects the accuracy of remote sensing products.

In this study, we first analyze whether GLADS-Noah ET_a can produce results that are compatible with station P-M results in the MRB. Meanwhile, we use the GLDAS-Noah ET_a data to describe the spatio-temporal patterns of ET_a. Then, we explore the influencing factors of ET_a spatio-temporal variability in the MRB.

2. Study Area, Dataset and Methods

2.1. Study Area

The MRB is located at 25°23′ N–28°19′ N, 116°23′ E–119°43′ E (Figure 1), with an area of 6.1×10^4 km^2, a total length of 562 km and an average annual runoff of 940 mm. The MRB belongs to the subtropical monsoon climate zone, with an average annual rainfall of 1600–1800 mm and annual temperature 16–20 °C [20]. The MRB has a forestland area of 4.15×10^4 km^2, and a cultivated land area of 0.92×10^4 km^2.

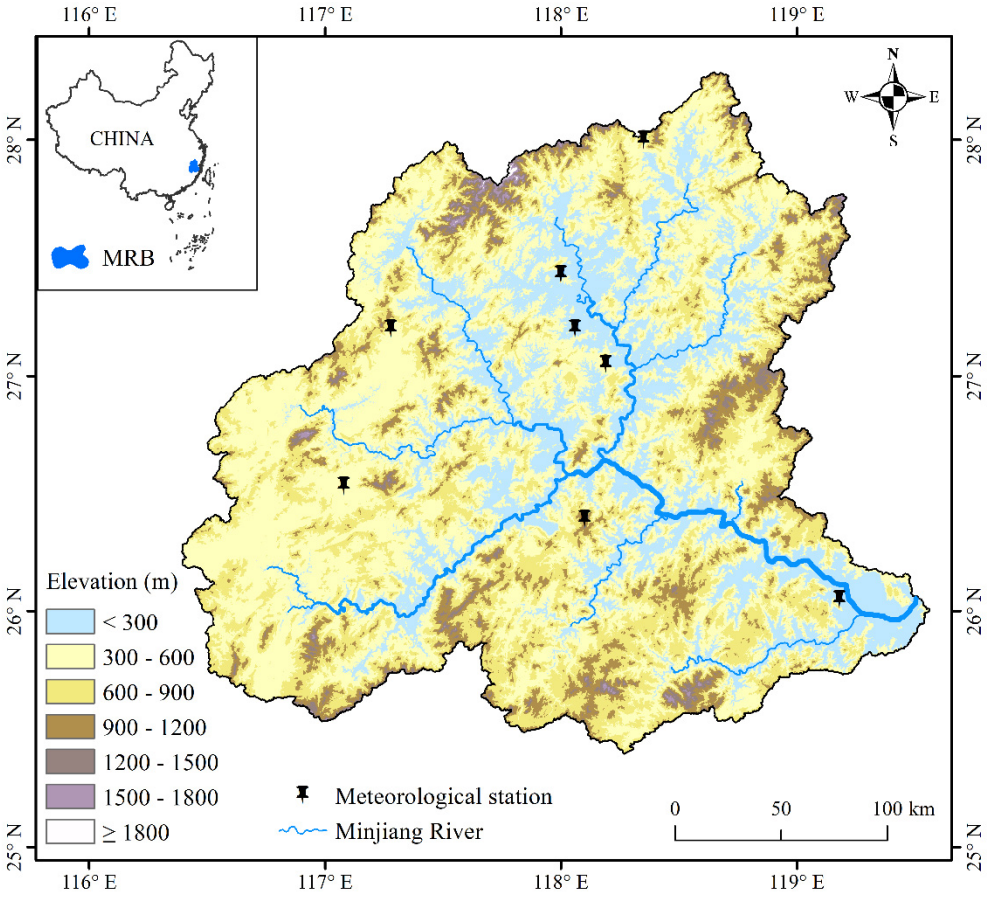


Figure 1. Topography and river network of the Minjiang River Basin (MRB).

2.2. Data Sources

2.2.1. Meteorological Data

Meteorological data used in this study come from the National Meteorological Information Center. In the study area, the daily data from eight meteorological stations (Table 1) during January 2000–December 2019 were collected, including the average, maximum and minimum temperature, precipitation, relative humidity, and hours of sunshine. The ET_a of the eight meteorological stations can be calculated based on these daily observation data.

Table 1. Basic information of the eight meteorological stations.

Name	Lat. (°N)	Lon. (°E)	ELev. (m)	Pre. (mm)	Temp. (°C)	LUCC
Shaowu	27	117	218	1855	18.3	Grass land
Wuyishan	27	118	222	1899	18.7	Forest land
Pucheng	28	118	277	1756	18.0	Forest land
Jianyang	27	118	197	1663	18.6	Cultivated land
Jianou	27	118	155	1682	19.4	Forest land
Taining	26	117	343	1804	17.9	Forest land
Nanping	26	118	152	1611	20.1	Grass land

Note: 'Elev.' is elevation; 'Pre.' is average annual precipitation in 2000–2019; 'Temp.' is average annual precipitation in 2000–2019.

2.2.2. GLDAS-Noah Data

The GLDAS version 2.1 is forced by a combination of satellite-based and ground-based observation products, and this system uses advanced land surface modeling and data assimilation techniques to generate optimal fields of land surface states and fluxes [22]. The land surface model parameters include four categories: elevation, soils, vegetation type and

extent, and leaf area index [22]. Therefore, the study did not account for changes in land cover. Currently, the GLDAS data are used to drive four land surface models including Noah, catchment and community land surface models and the variable infiltration capacity (VIC) land surface model. In this research, we select the monthly ET_a and precipitation data with a spatial resolution of 0.25° × 0.25° from the GLDAS-Noah model during 2000–2019. Figure 2 shows that the basin average of monthly GLDAS-Noah precipitation is quite close to average of eight stations observations, and the determination coefficient (R^2) is 0.9, indicating that the monthly GLDAS-Noah precipitation products are effective in simulating the precipitation in the MRB.

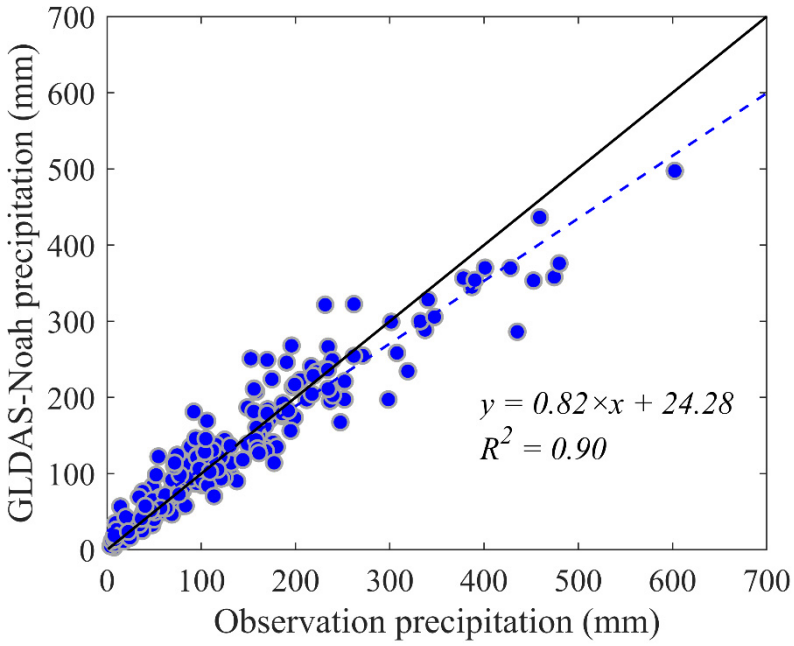


Figure 2. Scatter plot of monthly precipitation from station observations and the GLDAS-Noah in the MRB.

2.3. Method

2.3.1. Station ET_a Calculation

In this study, ET_a is calculated in two steps. Firstly, the *PET* of station is estimated by the P-M equation. Then, ET_a at station is calculated by combining the station PET with the dual crop coefficient.

$$ET_a = PET \times K_c \quad (1)$$

where ET_a is actual evapotranspiration, *PET* is potential evapotranspiration, and K_c is crop coefficient.

The P-M equation (Equation (2)) used to calculate *PET* in this study. Previous study indicated that P-M calculate *PET* are quite consistent with the measured values [23].

$$ET_0 = \frac{0.408\Delta(R_n - G) + r\frac{900}{T+273}U_2(e_s - e_a)}{\Delta + r(1 + 0.34U_2)} \quad (2)$$

where ET_0 indicates the *PET* (mm·day^{-1}), R_n the net radiation (MJ·m^{-2}·day^{-1}), G the soil heat flux density (MJ·m^{-2}·day^{-1}), T the 2-m air temperature (°C), U_2 the 2-m wind speed (m·s^{-1}), e_s the saturated water vapor pressure (kPa), e_a the actual vapor pressure (kPa), $e_s - e_a$ the saturated vapor pressure deficit (kPa), Δ the slope of vapor pressure curve (kPa·°C^{-1}), γ the psychrometric constant (kPa·°C^{-1}).

The method to calculated K_c was proposed by Wright in 1982 [24]. The previous study shows that the NDVI-based K_c values agree with the measured K_c values [25]. The K_c was calculated from NDVI and applied in this study.

$$K_c = K_s \times K_{cb} + K_e \tag{3}$$

$$K_{cb} = 1.07 \times \left[1 - \left(\frac{\mathrm{NDVI_{max}} - \mathrm{NDVI}}{\mathrm{NDVI_{max}} - \mathrm{NDVI_{min}}}\right)^{\frac{0.84}{0.54}}\right] \tag{4}$$

$$K_e = \beta \times (1 - f_c) \tag{5}$$

$$f_c = 1.3514 \times \mathrm{NDVI} - 0.2811 \tag{6}$$

where K_{cb} the basic crop coefficient reflecting the crop evapotranspiration, and K_e the evapotranspiration coefficient reflecting the soil surface evaporation. K_s represents the water stress coefficient reflecting the effect on the crop evapotranspiration when the soil water content in the root zone is insufficient (K_s = 1 means water is not a limiting factor) [26]. In this study, the value of K_s is taken as 1 because the MRB is a subtropical monsoon zone, so there is sufficient water. NDVI indicates the vegetation index, which is from NOAA Global Inventory Monitoring and Modeling System, where $\mathrm{NDVI_{max}}$ and $\mathrm{NDVI_{min}}$ are the maximum and minimum values of monthly NDVI from 2000 to 2014, respectively. f_c denotes the effective area ratio of vegetation covering the soil surface, β an empirical coefficient depending on the K_c values at the early and middle stages of crop growth. Based on previous research results [26], β is taken as 0.25 in this study.

2.3.2. Evaluation Metrics

In this study, we use a new comprehensive index DISO (distance of indices between simulation and observation) [27], R^2 and Nash-Sutcliffe efficiency coefficient (*NSE*) to evaluate the applicability of the GLDAS-Noah $\mathrm{ET_a}$ data in the MRB. The DISO can characterize the performance of the simulated data evaluated based on the distance between the simulated and the observed data [27]. The Smaller the DISO value, the higher the accuracy of the GLDAS-Noah $\mathrm{ET_a}$ data. The expression is as follows (Equation (6)).

$$\mathrm{DISO} = \sqrt{\mathrm{NRMSE}^2 + \mathrm{RB}^2 + (R-1)^2} \tag{7}$$

where NRMSE, RB and R are the normalized root mean square error, relative bias and Pearson correlation coefficient, respectively, which are calculated as follows.

$$\mathrm{NRMSE} = \frac{1}{\overline{\mathrm{OB}}}\sqrt{\frac{1}{n}\sum_{i=1}^{n}(\mathrm{SI}_i - \mathrm{OB}_i)^2} \tag{8}$$

$$\mathrm{RB} = \frac{\frac{1}{n}\sum_{i=1}^{n}(\mathrm{SI}_i - \mathrm{OB}_i)}{\frac{1}{n}\sum_{i=1}^{n}\mathrm{OB}_i} = \frac{\sum_{i=1}^{n}(\mathrm{SI}_i - \mathrm{OB}_i)}{\sum_{i=1}^{n}\mathrm{OB}_i} \tag{9}$$

$$R = \frac{\sum_{i=1}^{n}\left(\mathrm{SI}_i - \overline{\mathrm{SI}}\right)\left(\mathrm{OB}_i - \overline{\mathrm{OB}}\right)}{\sqrt{\sum_{i=1}^{n}\left(\mathrm{SI}_i - \overline{\mathrm{SI}}\right)^2}\sqrt{\sum_{i=1}^{n}\left(\mathrm{OB}_i - \overline{\mathrm{OB}}\right)^2}} \tag{10}$$

where OB denotes the results from the P-M method at the station, SI the GLDAS-Noah data, n the time series, $\overline{\mathrm{OB}}$ the mean of OB, and $\overline{\mathrm{SI}}$ the mean of SI.

The *NSE* (Equation (10)) is usually used to assess the fit of the simulated values to the observed values, and *NSE* values range from 0 to 1.

$$NSE = 1 - \frac{\sum_{1}^{n}(\mathrm{OB}_i - \mathrm{SI}_i)^2}{\sum_{1}^{n}\left(\mathrm{OB}_i - \overline{\mathrm{OB}}\right)^2} \tag{11}$$

Therefore, if the DISO is close to 0, the R^2 and *NSE* values are close to 1, this is indication that the simulation performance of the GLDAS-Noah model is relatively better.

2.3.3. Partial Least-Squares (PLS) Regression Model

In this study, we used the PLS regression model to estimate the impacts of climate variables (precipitation, temperature, and wind speed) on the ET_a, and determine the contribution of each climate variables.

$$ET_a = a + b \times P + c \times T + d \times W \tag{12}$$

where a, b, c, and d are regression coefficients; P, T, and W are standardization of precipitation, temperature, and wind speed, respectively. Once the regression coefficients of this equation were defined, we used the function to analysis the relative contribution of each climate variables on ET_a [28,29].

$$\begin{cases} \rho_p = |b| / (|b| + |c| + |d|) \\ \rho_T = |c| / (|b| + |c| + |d|) \\ \rho_W = |d| / (|b| + |c| + |d|) \end{cases} \tag{13}$$

where ρ_P, ρ_T, and ρ_W are relative contribution of precipitation, temperature, and wind speed on the ET_a.

3. Results

3.1. Applicability Assessment of the GLDAS-Noah ET_a Data

For the applicability assessment of ET_a data, the calculated results from the P-M equation at seven stations are used as observations, and the GLDAS-Noah ET_a data in the corresponding grid points at the stations are taken as simulations. The results (Table 2) show that the DISO for each station is less than 0.3, the *NSE* is greater than or equal to 0.8, and the R^2 values are all greater than 0.9. Thus, these results indicated that there is highly consistence between stations P-M result and GLDAS-Noah ET_a data in the corresponding grid points of meteorological stations.

Table 2. Applicability assessment of the GLDAS ET_a data.

Name	R^2	NSE	DISO
Shaowu	0.93	0.91	0.16
Wuyishan	0.92	0.90	0.16
Pucheng	0.93	0.82	0.29
Jianyang	0.94	0.93	0.15
Jianou	0.94	0.85	0.25
Taining	0.93	0.85	0.23
Nanping	0.92	0.80	0.26

Figure 3a shows that the GLDAS-Noah ET_a agrees with the station P-M ETa. Although the GLDAS-Noah ET_a underestimates the actual evapotranspiration, the Pbias is less than 15%. Meanwhile, the decidability coefficient of monthly GLDAS-Noah ET_a and station P-M results reaches 0.97 (Figure 3b). Therefore, the GLDAS-Noah ETa data have good applicability in the MRB and can assess the ET_a variation characteristics in this region.

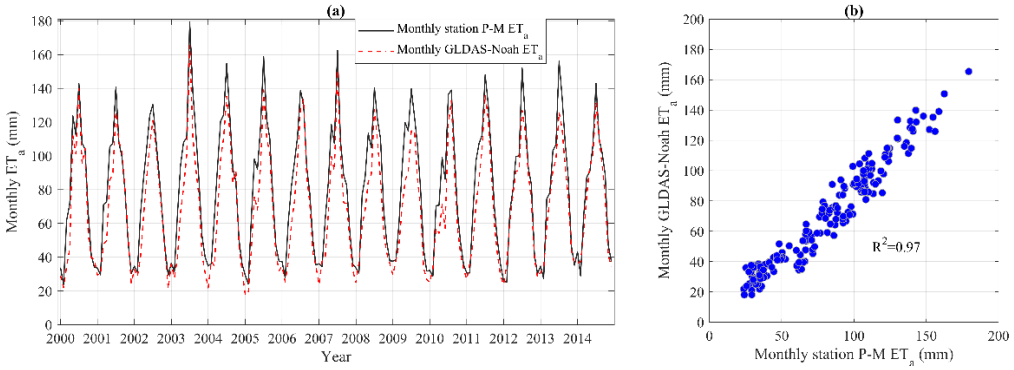


Figure 3. The compared analysis of monthly ET_a between average of egiht stations P-M results and GLDAS-Noah data over MRB in 2000–2019 as (**a**) time series and (**b**) as a scatter plot.

3.2. Spatio-Temporal Variations of the ET_a

During 2000–2019, ET_a in the MRB shows an increasing trend, and the overall increasing rate is 3.60 mm·yr^{-1}, passing the significance test of 0.01 confidence level (i.e., $p < 0.01$ as shown in Table 3). This result is consistent with the findings of Huang (2020) [30]. Moreover, there is a significant seasonal variation in the ET_a in the MRB. Winter includes December, January and February (DJF), spring for March, April, and May (MAM), summer for June, July and August (JJA), and autumn for September, October and November (SON). As expected, the largest ET_a occurs in summer (multi-year average of 342.1 mm), followed by spring and autumn (multi-year average of approximately 200 mm), and the smallest in winter (multi-year average of 92.6 mm). Most of the increasing trends in ET_a is occurring during the Spring months (2.60 mm yr^{-1}, $p < 0.01$). Interesting that a significant amount is happening during winter (1.10 mm yr^{-1}, $p < 0.01$). However, the ET_a variations in summer and autumn are nonsignificant.

Table 3. The annual and seasonal ET_a trend (by M-K trend test) in the MRB from 2000 to 2019.

	Mean Value (mm)	Trend (mm yr^{-1})
Annual	846.2	3.60 **
Winter	92.6	1.10 **
Spring	207.5	2.60 **
Summer	342.1	0.19
Autumn	202.5	−0.10

"**" indicate that the results passing the significance test at the 0.01 confidence level ($p < 0.01$).

The multi-year average ET_a in the MRB ranges from 700 mm to 1100 mm, regional average is 846 mm (Figure 4a). The average annual ET_a of GLDAS-Noah is reasonable, because of average annual precipitation range of 1600–1800 mm and annual runoff depth is about 900 mm. The annual ET_a generally shows increasing trends in the entire MRB during 2000–2019 (Figure 4b), except for slightly decreasing trends in individual grid points which indicate that ET_a tends to increases of most region in this basin under the background of climate warming. ET_a increasing rates above 4 mm·yr^{-1} pass the significance test at the 0.05 confidence level, while ET_a decreasing trends are nonsignificant. Moreover, the spatial differences in annual ET_a increase are obvious, with the most apparent increasing trend in the southwestern and southern parts of the MRB and weaker increasing trends in the central and northern parts.

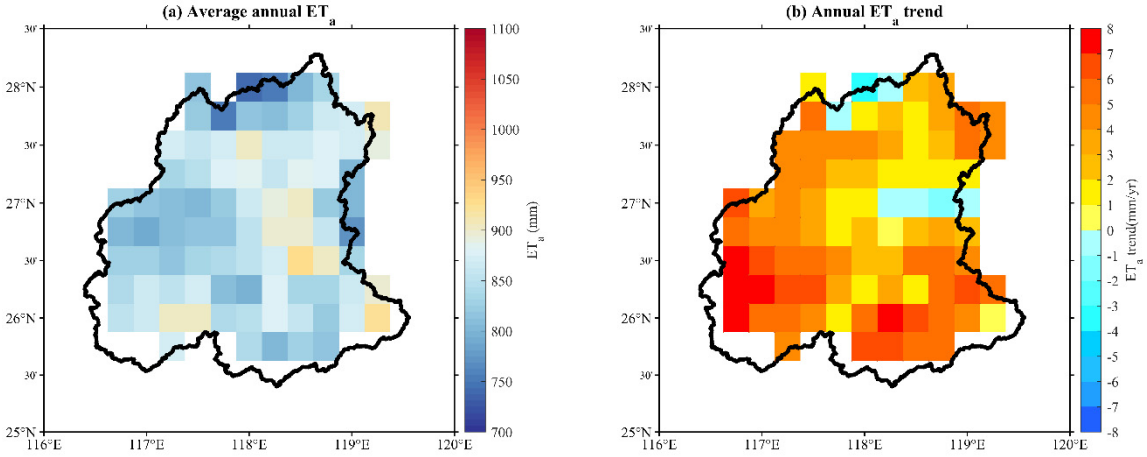


Figure 4. Average annual ET_a (**a**) and its trends (**b**) in the MRB from 2000 to 2019, and grid at 0.25° × 0.25°. The black dots in Figure 3b indicate that the variation rates passing the significance test (M-K trend test) at the 0.05 confidence level.

The spatial change in the ET_a seasonal variations in the MRB is obvious. There are generally significant increasing trends of ET_a ($p < 0.05$) in winter and spring throughout the basin. Specifically, the increasing rates in winter range from 1 mm·yr^{-1} to 2 mm·yr^{-1}, and the increasing rates are most significant in spring, with 2–4 mm·yr^{-1} in most areas (Figure 4b). The spatial differences in the ET_a variations in summer and autumn are noticeable. In summer, there are increasing trends ($p < 0.05$) from 2000 to 2019 in the southwestern and southeastern regions of the basin, while trends in the central and northern regions are decreasing but nonsignificant (Figure 4). In autumn, the ET_a tends to increase (0–1 mm yr^{-1}) in the western and southern parts of this region (Figure 5) and decrease (−1–0 mm yr^{-1}) in northeastern parts. However, none of these variation rates pass the significance test at the 0.05 confidence level.

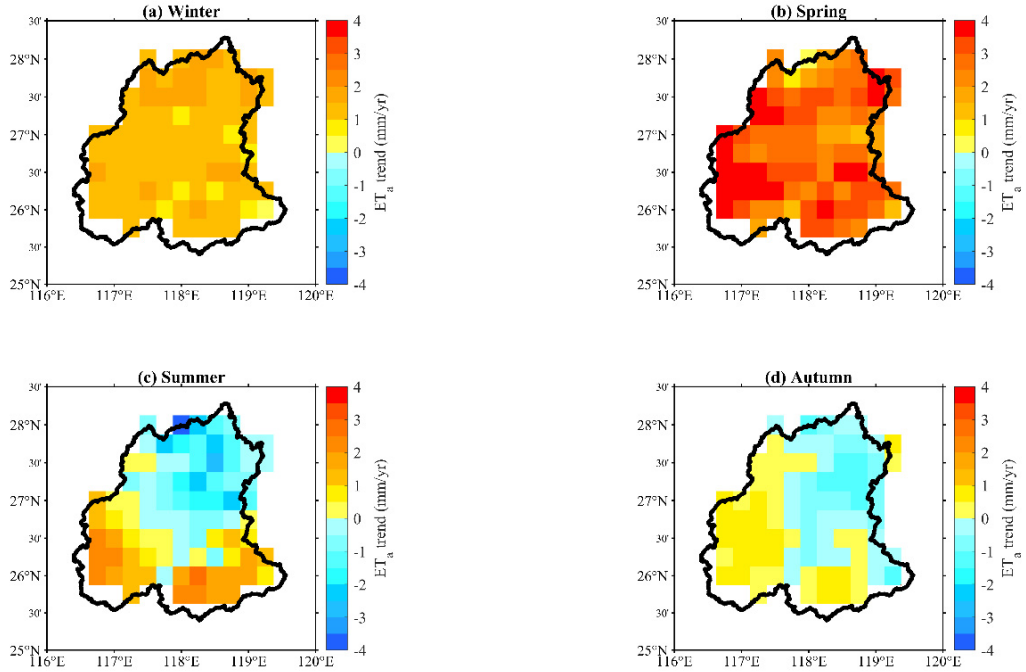


Figure 5. Seasonal trends of ET_a in the MRB in (**a**) winter, (**b**) spring, (**c**) summer and (**d**) autumn from 2000–2019, and grid at 0.25° × 0.25°.

3.3. Attribution Analysis of ET_a Variations in the MRB

Table 4 shows that annual ET_a was positively related to air temperature ($r = 0.35$) and negatively related to precipitation ($r = -0.20$). Annual wind speed had little effect on annual ET_a in the region. ET_a in winter was negatively related to precipitation ($r = -0.35$) and wind speed ($r = -0.24$). The spring ET_a was controlled by air temperature ($r = 0.60$, $p < 0.01$). Summer ET_a was controlled by precipitation ($r = -0.52$, $p < 0.05$) and air temperature ($r = 0.45$, $p < 0.05$). Autumn ET_a was weakly negatively related to precipitation ($r = -0.44$, $p < 0.1$).

Table 4. The Pearson correlation coefficients of between climate variables and ET_a from 2000 to 2019.

	Precipitation	Temperature	Wind Speed
Annual ET_a	−0.20	0.35	−0.08
Winter ET_a	−0.35	0.16	−0.24
Spring ET_a	−0.10	0.60 ***	−0.14
Summer ET_a	−0.52 **	0.45 **	0.26
Autumn ET_a	−0.44 *	−0.21	−0.10

Note: "***" indicate that the results passing the significance test at the 0.01 confidence level ($p < 0.01$), "**" denotes that the results passing the significance test at the 0.05 confidence level ($p < 0.05$), and "*" means that the results passing the significance test at the 0.1 confidence ($p < 0.1$).

To quantify the effects of climatic variables on ET_a in the MRB, we conduct PLS regression model. The PLS regression coefficient in Table 5 shows that precipitation, air temperature, and wind speed have seasonal differences. Annual air temperature has the largest effect on annual ET_a (59.6%). ET_a was mainly influenced by precipitation (64%) and wind speed (35.5%) in winter. ET_a increased (1.10 mm yr^{-1}, $p < 0.05$) in winter was due to increased precipitation and wind speed. In spring, ET_a is dominated by air temperature (89.4%). ET_a changes in summer and autumn are influenced by precipitation, with a relative contribution is 59.8% and 54.9%, respectively.

Table 5. PLS regression coefficient and relative contribution rates of climatic variables over MRB in 2000–2019.

	b	c	d	ρ_P	ρ_T	ρ_W
Annual	−0.20	0.35	−0.04	33.9%	59.6%	6.5%
Winter	−0.31	0.002	−0.17	64%	0.5%	35.5%
Spring	0.06	0.61	−0.01	8.6%	89.4%	2.0%
Summer	−0.40	0.17	0.10	59.8%	24.8%	15.5%
Autumn	−0.53	−0.20	−0.23	54.9%	21.0%	24.1%

4. Discussion

Evapotranspiration is one of critical processes in land-atmosphere interactions. The extrapolation of the ET_a estimation at a station to regional scale can result in significant errors. The reason for this is that the differences of underlying surfaces can lead to variations of meteorological elements, which consequently cause regional ET_a differences [31]. With the improvement of the Earth system observation capability, especially the continuous advancement of high-precision remote sensing technology [32,33]. Moreover, with the development of land surface models [34], such as the GLDAS-Noah and Famine Early Warning Systems Network Land Data Assimilation System of the Noah-MP land surface model, they can provide the ET_a from the land surface. Previous studies have extensively verified the applicability of GLDAS ET_a data in China. The monthly GLDAS ET_a had high stability and reliability in southwestern China [35]. In the Yellow River Basin, although there is little difference between GLDAS ETa and watershed ET_a based on water balance, the overall uncertainty is high [36]. In the Weihe River Basin, the GLDAS ET_a data products are fully meeting the needs of evapotranspiration research and have excellent application [37]. In the Yangtze River Basin, comparing the commonly used evapotranspiration data such as

GLEAMV3.2a, MOD16, and GLDAS-Noah 2, suggests that the error of the GLDAS-Noah 2 dataset is small [38].

The factors of ET_a variations can be divided into two categories: water limitation and energy limitation [2]. Water limitation mainly occurs in arid and semiarid areas, and energy limitation mainly occurs in humid climate areas [9]. ET change is more influenced by increased wind speed than the increased temperature in southern Italy [5]. In Canadian grasslands, wind speed significantly influences the decreasing evapotranspiration, while water vapor pressure difference (VPD) controls the increasing evapotranspiration [6]. In the Heihe River Basin of China, the most significant influencing factor on the daily variation of evapotranspiration is air humidity, followed by wind speed and soil moisture [7]. In the Jinsha River Basin, evapotranspiration is more sensitive to precipitation and temperature, followed by wind speed [8]. MRB is located in a subtropical monsoon zone, with an annual rainfall amount of about 1800 mm and an ET_a of approximately 846 mm. The ET_a variation in this region depends on energy limitation (Table 4), while a seasonal difference. In the context of global warming, the temperature in the MRB also tends to increase (0.3 °C·decade^{-1}, Table 6) from 2000 to 2019, which is an indicator of the increase in the energy term at the higher temperature. Meanwhile, precipitation also increased (~18–19 mm yr^{-1}) and wind speed insignificantly changed in the MRB. Therefore, combining Tables 4–6, the increase in ET_a in winter and spring in the MRB is mainly due to the rise in temperature and wind speed. The increase in ET_a was insignificant in summer, and it may be due to precipitation increases suppressed the effect of temperature rise on ET_a. There was a weakly decreasing trend of ETa in autumn, and although the temperature increased, wind speed did not change in autumn.

Table 6. Trend rate of ET_a, precipitation, air temperature, and wind speed in the MRB from 2000 to 2019.

	Precipitation (mm yr^{-1})	Temperature (°C yr^{-1})	Wind Speed (m yr^{-1})
Annual	18.56	0.03 *	−0.001
Winter	0.40	0.01	0.005
Spring	5.98	0.01	0.002
Summer	6.39	0.02	0.001
Autumn	0.37	0.06 **	0.000

Note: "**" denotes that the results passing the significance test at the 0.05 confidence level ($p < 0.05$), and "*" means that the results passing the significance test at the 0.1 confidence ($p < 0.1$).

In addition, the input parameters of the current GLDAS-Noah model do not include land-use types, which is an important reason that the GLDAS-Noah model underestimates the ET_a in the urban region. Therefore, our subsequent research will investigate the influence of vegetation changes on ET_a in the MRB.

5. Conclusions

In this study, we evaluated the applicability of the GLDAS-Noah ET_a data and then used the GLDAS-Noah products to analyze the ET_a variations in the MRB from 2000 to 2019. The main conclusions are as follows.

The accuracy of the GLDAS-Noah ET_a data was assessed by using the calculated results from the P-M equation in 2000–2019 at eight stations of the MRB. The assessment results showed that the GLDAS-Noah ET_a data had applicability in the MRB. The R^2 value was close to 1, the *NSE* value was larger than 0.8, and the DISO was less than 0.3, which indicated that the GLDAS-Noah ETa data could be used to analyze the ET_a variations in the MRB.

Since 2000, there have been significant spatio-temporal differences in the ET_a variations in the MRB. During 2000–2019, ET_a in the MRB shows an increasing trend, and the overall increasing rate is 3.60 mm·yr^{-1} ($p < 0.01$). The ET_a showed a significant increase in winter and spring, with increasing rates of 1.10 mm·yr^{-1} ($p < 0.01$) and 2.60 mm·yr^{-1} ($p < 0.01$), respectively, while the ET_a did not change significantly in other seasons. Spatially, the ET_a

tended to increase in winter and spring in the whole MRB. Therefore, we should pay more attention to the relationship between increased winter and spring ETa and the increased frequency of winter and spring droughts in the MRB, as well as the seasonal contradiction between supply and demand of water resources in the basin.

In the MRB, annual ET_a was positively related to air temperature ($r = 0.35$) and negatively related to precipitation ($r = -0.20$). There are seasonal differences in precipitation, air temperature, and wind speed that affect ET_a. ET_a was mainly influenced by precipitation (64%) and wind speed (35.5%) in winter. In spring, ET_a is dominated by air temperature, and the relative contribution rate of 89.4%.

Author Contributions: Conceptualization, H.D. and Q.L.; methodology, Y.L., Y.W. and H.D.; validation, X.C., Y.Z. and L.G.; formal analysis, Q.L., Y.C. and M.L.; writing—original draft preparation, Y.L. and Y.W.; writing—review and editing, H.D., Q.L., X.C., Y.Z., L.G., Y.C. and M.L. All authors have read and agreed to the published version of the manuscript.

Funding: This research was supported by the Projects for National Natural Science Foundation of China (41877167), and the National Key Research and Development Program (2018YFE0206400).

Institutional Review Board Statement: Not applicable.

Informed Consent Statement: Not applicable.

Data Availability Statement: The datasets generated and analyzed during the current study are not publicly available but are available from the corresponding author on reasonable request.

Acknowledgments: The air temperature, precipitation, air pressure, wind speed and relative humidity data are supported by the China Meteorological Data Service Center. The authors appreciate the comments and encouragement given by the reviewers, editor, and associate editor.

Conflicts of Interest: The authors declare no conflict of interest.

References

1. Gan, G.; Liu, Y.; Sun, G. Understanding interactions among climate, water, and vegetation with the Budyko framework. *Earth-Sci. Rev.* **2021**, *212*, 103451. [CrossRef]
2. Roderick, M.L.; Farquhar, G.D. The Cause of Decreased Pan Evaporation over the Past 50 Years. *Science* **2002**, *298*, 1410–1411. [CrossRef] [PubMed]
3. Beven, K. A sensitivity analysis of the Penman-Monteith actual evapotranspiration estimates. *J. Hydrol.* **1979**, *44*, 169–190. [CrossRef]
4. Zeng, R.; Cai, X. Assessing the temporal variance of evapotranspiration considering climate and catchment storage factors. *Adv. Water Resour.* **2015**, *79*, 51–60. [CrossRef]
5. McCabe, M.F.; Rodell, M.; Alsdorf, D.E.; Miralles, D.G.; Uijlenhoet, R.; Wagner, W.; Lucieer, A.; Houborg, R.; Verhoest, N.E.C.; Franz, T.E.; et al. The future of Earth observation in hydrology. *Hydrol. Earth Syst. Sci.* **2017**, *21*, 3879–3914. [CrossRef]
6. Bowen, I.S. The ratio of heat losses by conductions and by evaporation from any water surface. *Phys. Rev.* **1926**, *27*, 779–787. [CrossRef]
7. Shuttleworth, W.J.; Wallace, J.S. Evaporation from sparse crops-an energy combination theory. *Q. J. R. Meteorol. Soc.* **1985**, *111*, 839–855. [CrossRef]
8. Zhang, B.; Xu, D.; Liu, Y.; Chen, H. Review of multi-scale evapotranspiration estimation and spatio-temporal scale expansion. *Trans. Chin. Soc. Agric. Eng.* **2015**, *31*, 8–16. (Chinese with English Abstract)
9. Liu, Y.; Qiu, G.; Zhang, H.; Yang, Y.; Zhang, Y.; Wang, Q.; Zhao, W.; Jia, L.; Ji, X.; Xiong, Y.; et al. Shifting from homogeneous to heterogeneous surfaces in estimating terrestrial evapotranspiration: Review and perspectives. *Sci. China Earth Sci.* **2022**, *65*, 197–214. [CrossRef]
10. Guerschman, J.P.; McVicar, T.R.; Vleeshower, J.; Van Niel, T.G.; Peña-Arancibia, J.L.; Chen, Y. Estimating actual evapotranspiration at field-to-continent scales by calibrating the CMRSET algorithm with MODIS, VIIRS, Landsat and Sentinel-2 data. *J. Hydrol.* **2021**, *605*, 127318. [CrossRef]
11. Yin, Y.; Wu, S.; Dai, E. Determining factors in potential evapotranspiration changes over China in the period 1971–2008. *Chin. Sci. Bull.* **2010**, *55*, 3329–3337. [CrossRef]
12. Wen, S.; Jiang, T.; Li, X.; Wang, T.; Wang, Y.; Thomas, F. Changes of actual evapotranspiration over the Songhua River Basin from 1961 to 2010. *Adv. Clim. Chang. Res.* **2014**, *10*, 79–86. (Chinese with English Abstract)
13. Mo, X.; Chen, X.; Hu, S.; Hu, S.; Liu, S.; Xia, J. Attributing regional trends of evapotranspiration and gross primary productivity with remote sensing: A case study in the North China Plain. *Hydrol. Earth Syst. Sci.* **2017**, *21*, 295–310. [CrossRef]

14. Liu, Y.; Zhou, M.; Chen, Z.; Li, S. Sensitivity of the potential evapotranspiration to climate and vegetation in Hanjiang River basin based on S-W Model. *Trans. Chin. Soc. Agric. Eng.* **2013**, *29*, 92–100. (Chinese with English Abstract)
15. Zhao, Y.; Zou, X.; Zhang, J.; Cao, L.; Xu, X.; Zhang, K.; Chen, Y. Spatio-temporal variation of reference evapotranspiration and aridity index in the Loess Plateau Region of China, during 1961–2012. *Quat. Int.* **2014**, *349*, 196–206. [CrossRef]
16. Ma, N.; Zhang, Y. Increasing Tibetan Plateau terrestrial evapotranspiration primarily driven by precipitation. *Agric. For. Meteorol.* **2022**, *317*, 108887. [CrossRef]
17. Zhao, Y.; Zou, X.; Cao, L.; Yao, W.; Fu, J. Spatiotemporal variations of potential evapotranspiration and aridity index in relation to influencing factors over Southwest China during 1960–2013. *Theor. Appl. Climatol.* **2018**, *133*, 711–726. [CrossRef]
18. Li, Z.; Chen, Y.; Shen, Y.; Liu, Y.; Zhang, S. Analysis of changing pan evaporation in the arid region of Northwest China. *Water Resour. Res.* **2013**, *49*, 2205–2212. [CrossRef]
19. Liu, C.; Zhang, D. Temporal and spatial change analysis of the sensitivity of potential evapotranspiration to meteorological influencing factors in China. *Sci. Geogr. Sin.* **2011**, *66*, 579–588. (Chinese with English Abstract)
20. Chen, Y.; Chen, X.-W.; Yin, Y.-X. Characteristics of Runoff Changes in the Minjiang River Basin from 1960 to 2006. *J. Nat. Resour.* **2011**, *26*, 1401–1411.
21. Huang, W.; Sui, Y.; Yang, X.; Wei, D.; Song, L. Characteristics and adaptation of seasonal drought in southern China under the background of climate change.III. Spatiotemporal characteristics of seasonal drought in southern China based on the percentage of precipitation anomalies. *Chin. J. Appl. Ecol.* **2013**, *24*, 397–406. (Chinese with English Abstract)
22. Rodell, M.; Houser, P.R.; Jambor, U.; Gottschalck, J.; Bosilovich, M. The Global Land Data Assimilation System. *Bull. Am. Meteorol. Soc.* **2004**, *85*, 381–394. [CrossRef]
23. Zhao, L.; Ji, X. Quantification of transpiration and evaporation over agricultural field using the FAO-56 dual crop coefficient approach—A case study of the maize field in an oasis in the middlestream of the Heihe River Basin in northwest China. *Sci. Agric. Sin.* **2010**, *43*, 4016–4026. (Chinese with English Abstract)
24. Wright, J.L. New evapotranspiration crop coefficients. *Proc. Am. Soc. Civ. Eng. J. Irrig. Drain. Div.* **1982**, *108*, 57–74. [CrossRef]
25. Baburao, K.; Ayse, K.; Kenneth, H. Estimating Crop Coefficients Using Remote Sensing-Based Vegetation Index. *Remote Sens.* **2013**, *5*, 1588–1602. [CrossRef]
26. Rocha, J.; Perdigo, A.; Melo, R.; Henriques, C. Managing water in agriculture through remote sNSEing applications. In Proceedings of the 30th EARSeL Symposium on Remote Sensing for Science, Education, and Natural and Cultural Heritage, Paris, France, 31 May–3 June 2010; Volume 31, p. 223230. [CrossRef]
27. Hu, Z.; Chen, X.; Zhou, Q.; Chen, D.; Li, J. DISO: A rethink of Taylor diagram. *Int. J. Climatol.* **2019**, *39*, 2825–2832. [CrossRef]
28. Hu, Z.; Zhang, Z.; Sang, Y.-F.; Qian, J.; Feng, W.; Chen, X.; Zhou, Q. Temporal and spatial variations in the terrestrial water storage across Central Asia based on multiple satellite datasets and global hydrological models. *J. Hydrol.* **2021**, *596*, 126013. [CrossRef]
29. Zhang, S.H.; Liu, S.X.; Mo, X.G.; Shu, C.; Sun, Y.; Zhang, C. Assessing the impact of climate change on potential evapotranspiration in aksu river basin. *J. Geogr. Sci.* **2011**, *21*, 609–620. [CrossRef]
30. Huang, Q.; Qiu, Y.; Chen, X.; Sun, X.; Lin, Y. Climate Change Characteristics and Future Trends of Fujian Province during 1980—2017. *J. Wuyi Univ.* **2020**, *39*, 27–32. (Chinese with English Abstract)
31. Ramillien, G.; Frappart, F.; Güntner, A.; Ngo-Duc, T.; Cazenave, A.; Laval, K. Time variations of the regional evapotranspiration rate from Gravity Recovery and Climate Experiment (GRACE) satellite gravimetry. *Water Resour. Res.* **2006**, *42*, 10403-1–10403-8. [CrossRef]
32. Mu, Q.; Zhao, M.; Running, S.W. Improvements to a MODIS global terrestrial evapotranspiration algorithm. *Remote Sens. Environ.* **2011**, *115*, 1781–1800. [CrossRef]
33. Rodell, M.; Famiglietti, J.S.; Chen, J.; Seneviratne, S.I.; Viterbo, P.; Holl, S.; Wilson, C.R. Basin scale estimates of evapotranspiration using GRACE and other observations. *Geophys. Res. Lett.* **2004**, *31*, L20504. [CrossRef]
34. Di, L.; Longuevergne, L.; Scanlon, B.R. Uncertainty in evapotranspiration from land surface modeling, remote sensing, and GRACE satellites. *Water Resour. Res.* **2014**, *50*, 1131–1151. [CrossRef]
35. Li, H.; Wang, S.; Bai, X.; Tang, H.; Cao, Y.; Wang, M.; Wu, L. Inversion and Spatiotemporal Evolution of Actual Evapotranspiration in Southwest China for the Past 50 Years. *Acta Ecol. Sin.* **2018**, *38*, 8835–8848. [CrossRef]
36. Chen, X.; Deng, C. Evaluation and Integration of Multiple Evapotranspiration Products in the Yellow River Basin. *Water Resour. Power* **2021**, *39*, 5–8.
37. Wang, Y.; Wang, S.; Song, W.; Yang, S. Application of GLDAS Data to the Potential Evapotranspiration Monitoring in Weihe River Basin. *J. Arid Land Resour. Environ.* **2013**, *27*, 53–58. [CrossRef]
38. Zhan, Y.; Zhang, W.; Yan, Y.; Wang, C.; Rong, Y.; Zhu, J.; Lu, H.; Zheng, T. Analysis of actual evapotranspiration evolution and influencing factors in the Yangtze River Basin. *Acta Ecol. Sin.* **2021**, *41*, 6924–6935. [CrossRef]